



HAL
open science

Diffraction-limited mid-infrared microspectroscopy to reveal a micron-thick interfacial water layer signature

Armin Mozhdehei, Aneta Slodczyk, Eirik Almklov Magnussen, Achim Kohler, Christophe Sandt, Ferenc Borondics, Lionel Mercury

► **To cite this version:**

Armin Mozhdehei, Aneta Slodczyk, Eirik Almklov Magnussen, Achim Kohler, Christophe Sandt, et al.. Diffraction-limited mid-infrared microspectroscopy to reveal a micron-thick interfacial water layer signature. *Analyst*, 2023, 148 (13), pp.2941-2955. 10.1039/d3an00138e . insu-04190435

HAL Id: insu-04190435

<https://insu.hal.science/insu-04190435>

Submitted on 26 Oct 2023

HAL is a multi-disciplinary open access archive for the deposit and dissemination of scientific research documents, whether they are published or not. The documents may come from teaching and research institutions in France or abroad, or from public or private research centers.

L'archive ouverte pluridisciplinaire **HAL**, est destinée au dépôt et à la diffusion de documents scientifiques de niveau recherche, publiés ou non, émanant des établissements d'enseignement et de recherche français ou étrangers, des laboratoires publics ou privés.

Diffraction-limited mid-infrared microspectroscopy to reveal a micron-thick interfacial water layer signature

Armin Mozhddehei¹

Aneta Slodczyk^{1,2}

Eirik Almklov Magnussen³

Achim Kohler³

Christophe Sandt⁴

Ferenc Borondics⁴

Lionel Mercury¹

1. Institut des Sciences de la Terre d'Orléans - UMR 7327 Université d'Orléans, CNRS, BRGM - 45071 Orléans Cedex, France.

2. CEMHTI, UPR 3079 CNRS- Université d'Orléans, F-45071, Orléans, France.

3. Faculty of Science and Technology, Norwegian University of Life Sciences, Ås, Norway

4. Synchrotron Soleil, L'Orme des Merisiers Route départementale 128 – 91190 SAINT AUBIN, France

Abstract

Mid-infrared microspectroscopy is a non-invasive tool for identifying the molecular structure and chemical composition at the scale of the probe, i.e., at the scale of the beam. Consequently, investigating small objects or domains (commensurable to the wavelength) requires high-resolution measurements, even down to the diffraction limit. Herein, different protocols and machines allowing high-resolution measurements in transmission mode (aperture size (i.e., beam size) from $15 \times 15 \mu\text{m}$ to $3 \times 3 \mu\text{m}$) are tested using the same sample. The model sample is a closed cavity containing a water-air assemblage buried in a quartz fragment (fluid inclusion). The spectral range covers the water stretching band ($3000 - 3800 \text{ cm}^{-1}$), whose variations are followed as a function of the distance to the cavity wall. The experiments compare the performance of one focal plane array (FPA) detector associated with a Globar source with respect to a single-element mercury cadmium telluride (MCT) detector associated with a supercontinuum laser (SCL) or a synchrotron radiation source (SRS). This work also outlines the importance of post-experiments data processing, including interference fringes removal and Mie scattering correction, to ensure that the observed spectral signatures are not related to optical aberrations. We show that the SCL and the SRS-based setups detect specific spectral features along the quartz boundary (solid surface), invisible to the FPA imaging microscope. Additionally, the broadband SCL has thus the potential to substitute at the laboratory scale the SRS for conducting diffraction-limited high-resolution measurements.

1. Introduction

Mid-infrared microspectroscopy is a well-established, non-destructive method for high-resolution measurements, which enables chemical analysis of samples, qualitatively in general or quantitatively, up to diffraction-limited spatial resolution.¹ According to Abbe equation ($d = 1.22 \lambda / (2 \text{ NA})$), the diffraction-limited resolution is commensurable with the wavelength (λ) of the spectral region of interest and with the numerical aperture (NA) of the applied objective. Infrared microspectroscopy down to the diffraction limit has been widely applied to study biological samples in the past 40 years. It allowed exploring the individual cells for revealing the damage mechanisms and modification of protein structure,^{2, 3} diagnosing diseases,⁴⁻⁸ studying microbiology and bacteria,⁹⁻¹³ biochemical and biophysical modification processes,¹⁴⁻¹⁹ and variation of chemical composition.²⁰⁻²³ In all that, working at the diffraction limit was turned to downscale at the size of the individual biological object. Furthermore, this technique has been used in material science to investigate the charge dynamics in a single atomic layer of graphite,^{24, 25} in food industry for exploring the modification of protein structure,²⁶⁻²⁸ in astrophysics to probe the local geochemical conditions during aqueous alteration on the asteroid,²⁹ and in geoscience to map the distributions of organic matter, chemicals and minerals on a micrometer scale in geological samples surface.³⁰⁻³⁴ In these studies, the objective was to reach an spatial resolution commensurable to the chemical distribution or to the heterogeneity in a material. More recently, in earth science and porous media, our group started using the high-resolution infrared transmission microspectroscopy to explore the water behavior at a solid-liquid interface.³⁵ Probing interfaces is usually done through nonlinear techniques such as second-harmonic generation (SHG) or sum frequency generation spectroscopy (SFG),³⁶⁻⁴⁵ but we decided to apply the FTIR transmission microscopy according to classic linear spectroscopy. To increase the chance of getting specific spectral signatures near the interface, we targeted to use small beam, with size close to or at the diffraction limit.

In the mid-infrared microspectroscopy setups, optical arrangement of microscopes might have different modes, such as confocal, semi-confocal, and aperture-less. The standard confocal mode consists in positioning an aperture (mask) in front of the detector in the focal plane of the objective. The aperture defines the beam size, creating a diffraction pattern that limits the actual spatial resolution. Some studies have shown that the higher-order diffraction was limited by utilizing two apertures, the first between the sample and the detector and the second between the IR source and the sample, called dual confocal mode.^{46, 47} The dual confocal configuration allows the beam to be focused on the sample while eliminating most of the diffraction pattern, but it incurs tremendous photon losses degrading the signal-to-noise ratio (SNR).⁴⁷⁻⁵⁰ There is a strong dependency between spatial resolution, aperture size (field of view), NA of the objective, SNR, and acquisition time (number of scans). The final beam size and then the best spatial resolution achievable by a given equipment result from combining all these factors.⁵¹ In this way, a bigger aperture size is suggested for acquiring the hyperspectral data with high SNR at a shorter acquisition time. However, spatial resolution moves away from the diffraction limit.

In order to record high-resolution measurements down to the diffraction limit, an IR source with high brilliance and collimation is required. Generally, the classical mid-infrared microspectroscopy setup exploits thermal emitters (silicon carbide—Globar). In many studies, a Globar source works properly down to an aperture of around $15 \times 15 \mu\text{m}$; below this value, the SNR of the recorded spectrum decreases because of the low photon count.⁵²⁻⁵⁵ Since the Globar emission is not directional, most radiation is lost in all directions, and only a small fraction is collected efficiently in the microscope optics. Using a collimated infrared source such as an infrared laser or a synchrotron radiation source (SRS) allows for easier and more efficient collimation in the microscope optics and reduces photon losses.⁵³⁻⁵⁵

SRS use the property of charged particles that lose kinetic energy by emitting highly directional photon beams (emission of ‘Bremsstrahlung’ or ‘braking radiation’) when the particles are first accelerated at relativistic speeds and deviated in a magnetic field. Though a SRS can emit from the microwave to X-ray spectral regions, the Bremsstrahlung emission has several interesting properties, specifically for infrared microscopy: it covers an ultra-broadband spectral range from the Terahertz (mm wavelengths) to the near-infrared ($1 \mu\text{m}$ wavelength), and it can be efficiently collected and focused in microscope optics thanks to its small emission angle. This last feature makes the SRS a tool of choice to perform high-resolution mid-infrared microspectroscopy measurements. They allow to achieve the diffraction-limited spatial resolution (aperture size $3 \times 3 \mu\text{m}$) over the $3.33\text{--}2.63 \mu\text{m}$ range related to the OH stretching band of water (following the Abbe equation, the diffraction limit is $2.53 \mu\text{m}$ in the case of the $2.7 \mu\text{m}$ wavelength).^{35, 56-58} Meanwhile, owing to the recent development of infrared laser technology, the quantum cascade lasers (QCL) and supercontinuum generation of lasers (SCL) have been employed as an alternative high-brilliance infrared radiation source.^{51, 56, 59-64} QCL has enough power and brilliance to exploit an aperture size smaller than the wavelength of radiation and therefore perform high spatial resolution measurements.^{65, 66} However, QCL are discrete bandwidth sources, and so were not adapted to our study. SCL combines the primary benefits of a synchrotron light source, namely a high brilliance, high collimation, and diffraction-limited spatial resolution with broader bandwidth than the QCL in a compact structure. Obviously, the SCL spectral bandwidth is still limited compared to the ultra-broadband synchrotron sources.

Most mid-infrared microspectroscopy setups employ confocal microscopes and single-element mercury cadmium telluride (MCT) detectors. In this configuration, the hyperspectral maps are acquired via point-by-point measurements. However, another type of detector called focal plane array (FPA) comprises multiple small detector components organized in a two-dimensional grid on a focal plane. FPA-based systems produce high-definition spectral images (definition being the number of pixels in the image). Each pixel corresponds to the projected region of the sample and represents a distinct, full infrared spectrum.⁶⁷⁻⁷⁰

This paper aims to compare the efficiency of the mid-infrared microspectroscopy setups to deal with the interfacial water layer signatures in the light of previous synchrotron-based measurements revealing that liquid water can adopt specific infrared signatures along the water-quartz interfaces

within a micron-thick layer.³⁵ The test sample is an intra-mineral cavity, buried inside a quartz crystal with sharp solid walls, and containing a liquid-air mixture in a totally closed environment. The quartz fragment was double-side polished down to a 19 ± 1 μm thickness, and the cavity is located 4 μm beneath the top surface. This object is commonly called a fluid inclusion in Earth sciences, and offers optically sharp liquid-solid and liquid-air interfaces. Characterizing and quantifying the interfacial behavior requires recording mid-infrared transmission spectra at micron-scale in the OH stretching range of water (from 3000 to 3800 cm^{-1}) along precise and reproducible locations. The OH stretching band is very sensitive to changes in the network of hydrogen bonds among the water molecules.⁷¹ The frequency of vibration of the stretching mode is commonly linked to the distance between the two oxygen atoms of the O-H \cdots O bond.^{72, 73} As a result, it is possible to attribute an average length of the hydrogen bond to each vibration frequency.

To explore the particular behavior of liquid water near the interfaces, three terms will be used in this study: “normal water,” “bulk water,” and “interfacial water.” Normal water corresponds to water not located inside any closed media. Bulk water refers to the water located in the middle of a synthetic fluid inclusion, far away from any solid-liquid interface. Interfacial water is defined as water within a thick layer along a solid wall.

Since the interfacial signature may be modified over a sub-micron layer from the solid surface,^{74, 75} we need to perform the high-resolution measurements at the diffraction limit with as small as possible beam size regarding the SNR. In this way, four different experimental setups, based on three different infrared sources (Globar, SCL, and SRS), two optical arrangements (confocal and apertureless), and two detectors (MCT and FPA), are employed. Then, the hyperspectral data recorded with each experimental setup are compared in terms of SNR and spectral profiles (peak shape and position).

2. Material and Methods

2.1. Synthetic fluid inclusion as the case study

A series of microcavities in various crystalline hosts, the so-called fluid inclusions, are studied in our group. Their major advantages are: (i) their total closeness, (ii) the smoothness of the inner walls, (iii) often, the mineralogical equilibrium shape, evidenced by the negative crystal shape. Along the P-T conditions, liquid (water or solution) of known composition has a constant total volume, and follows either the monovariant saturation curve or the isochoric curve. The presence of the bubble is a chance to study the liquid-vapor interface, which is known to be hydrophobic.

For the present study, we used synthetic fluid inclusion (SFI), which was produced in a solid quartz crystal by hydrothermal synthesis.^{35,76} The quartz was chosen as a hosting mineral since it is poorly twinned, poorly soluble in saline solutions, and transparent in a wide range of electromagnetic radiation. The transparency is a crucial property for micro-FTIR measurements performed in the transmission mode.

Figure 1 illustrates the shape of the chosen SFI, which is a closed pore with constant composition and well-defined solid-liquid and liquid-gas interfaces. This geometry provides an opportunity to record the absorption signature of water and quartz at accurate positioning and capture any underlying mechanism existing at the frontiers between the two phases (interphase domain). As shown in Figure 1A, there are three different phases in the fluid inclusion: solid (quartz), liquid (water), and gas (bubble of saturated water vapor). The length, width, and depth of the SFI are 60, 20, and 5 μm , respectively. The diameter of the bubble is equal to 10 μm , and its depth is 5 μm . X-ray tomography measurements with sub-micron accuracy confirm the planar shape of the fluid inclusion and its dimension (Figure 1B).³⁵ It should be noted that all the mid-infrared microspectroscopy experiments are conducted with particular attention to the interfacial behavior of water located near the quartz boundary.

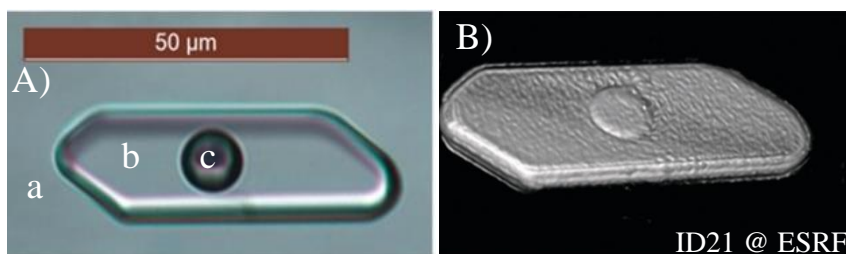


Figure 1. A) Micrographic image of the synthetic fluid inclusion including three different phases: a) solid (quartz), b) bulk water, and c) gas (bubble of saturated water vapor). B) X-ray tomography image of SFI at 0.5 μm spatial resolution (ID21 beamline, ESRF).³⁵

2.2. Experimental setups and conditions

Table 1 shows four different FTIR setups employed to explore the interfacial signature of water near the quartz boundary (water-solid interface) in the transmission mode. In setup I, the Global source was used with an FPA detector and an apertureless microscope. In setups II, III, and IV, we compared three infrared sources: Global, SCL, and the SRS, respectively, with the same MCT detector and confocal microscope. The confocal geometry was obtained using the same Continuum microscope which takes advantage of the catoptric design of the Schwarzschild objectives. They create a central obscuring of the incident beam below the primary mirror, a shadow, which prevents the radiation to collect most of the information outside the focal plane. The confocal arrangement is obtained by coupling that shadow with a special optical configuration called ‘single aperture dual path mode.’^{46, 77} This mode uses a single aperture, and confocality is obtained by passing the IR beam twice through it, once before the sample and once after crossing it. Actually, in transmission geometry, the shadow is present above and below the specimen placed at the confocal plan. This configuration allows confocal measurement, reduces diffraction, and improves X, Y, and Z spatial resolutions.^{46, 77} However, as the radiation crosses all the sample, we cannot exclude a contribution of the whole volume of water into the recorded signal in various, but likely small, proportions.

The main differences between the sources were their brilliance and collimation, which allowed us to obtain a high SNR (Table 1) at various beam sizes (from 15×15 to 3×3 μm). Experiments using setups I and IV were conducted at the SMIS beamline at the SOLEIL Synchrotron facility (Gif sur Yvette, France), whereas those based on setups II and III were performed at the Earth Sciences Institute of Orléans, ISTO (Orléans, France).

During all the mid-infrared microspectroscopy experiments (Table 1), the spectrum of water in the fluid inclusion was recorded in the OH stretching range. This is because the quartz cut-off occurred at the wavenumbers below 2000 cm^{-1} ; consequently, all low-wavenumber features were masked by the quartz absorption. The background spectrum was recorded through the surrounding quartz matrix before each set of spectra, to remove the effects of any changes in atmospheric CO₂ and water vapor. All spectra were recorded in transmission mode at 8 cm^{-1} spectral resolution with 256 scans. All spectra of bulk and near the interface, acquired with the four setups, are shown after processing, including baseline correction (by subtracting a linear baseline in the $2800 - 4200 \text{ cm}^{-1}$) and normalization using OriginPro v.2021 software. Moreover, the FFT filter method with 15-20 points of window was employed by using OriginPro v.2021 software for smoothing the bulk water spectra. In the case of the spectra recorded by setups III and IV, additional processing methods, such as interference fringe removal and Mie-scattering correction, were done by implementing an algorithm in Igor Pro 9.0 software and deep learning-based modelling, respectively. For the interference fringe removal, the method illustrated in Ref.⁷⁸, and for Mie-scattering correction, the method presented in Ref.⁷⁹ were applied to the raw spectra as described below. The SNR was calculated similarly to the method applied in [Ref.^{56, 80}] using the following equations:

$$\text{SNR} = \sqrt{n} \times \frac{S_{\text{average}}}{\sigma} = \sqrt{n} \times \frac{1}{\text{RMS}}$$

Where n is the number of scans, S_{average} is average absorbance value in the chosen spectral range, σ is standard deviation, corresponding to the differences between the highest and lowest absorbance value in the chosen spectral range, and RMS is root mean square of noise level.

In the case of setups II, III and IV, the 4000-4200 cm^{-1} spectral range, where no specific absorption peaks are present, was considered in the calculations. Exceptionally, for setup I, because of reduced spectral range available, the 2400-2600 cm^{-1} range was chosen.

Table 1. The detailed information of four FTIR experimental setups employed for recording the interfacial signature of water near the quartz boundary (water-solid interface) in transmission mode.

Setup	IR source	Spectrometer	Microscope	Microscope optical arrangement	Detector	The smallest beam size	Spectral range (cm^{-1})	Signal-to-noise ratio
I	Globalar	Cary 670	Cary 620 (Agilent)	Apertureless	Focal Plane Array (FPA)	0.65×0.65 (projected pixel size)	900-3950	241
II		Nicolet 6700	Nicolet Continuum	Confocal (single aperture dual path mode)	Single element mercury cadmium telluride (MCT)	15×15 μm	2800-4200	358
III	Supercontinuum laser (SCL)					5×5 μm		196
IV	Synchrotron (SRS)					Nicolet 8700		3×3 μm

2.2.1. Setup I

The set of infrared transmission spectral images was taken on a Cary 620 series FTIR apertureless microscope (Agilent, Courtaboeuf, France) equipped with a liquid-nitrogen cooled 128×128 pixels Lancer FPA detector and coupled to a Cary 670 FTIR spectrometer using a KBr beamsplitter and a Michelson interferometer with an internal source (Globalar). The microscope was equipped with a 25X objective ($\text{NA} = 0.81$) and matching condenser amplified by high magnification optics giving a final magnification of 62.5X. The FPA detector and the high magnification optics provide the theoretical projected pixel size of 0.65×0.65 μm and a field of vision of 84×84 μm .

2.2.2. Setup II

Setup II was based on a Continuum microscope coupled to a Nicolet 6700 FTIR spectrometer (Thermo Fisher Scientific, USA) with an internal source (Globar). The microscope was equipped with liquid-nitrogen cooled 50 μm MCT detector, a 32X infinity-corrected Schwarzschild type objective (NA = 0.65, WD = 7 mm, allowing a maximum beam size of 50 \times 50 μm), and a matching 32X condenser that worked in the confocal mode. Herein, the Continuum microscope uses the ‘single aperture dual path mode’ to obtain a confocal geometry. The minimum beam size acquired by this setup, is limited by the achievable SNR and the light transmittance value, is equal to 15 \times 15 μm .

2.2.3. Setup III

Setup III was based on setup II and had the same configuration except for the IR source. In this setup, the unpolarized supercontinuum laser (Coverage®, Novae, Limoges, France) was employed as an infrared source.^{64, 81} Coverage® is a turn-key supercontinuum source that emits a continuous spectrum from 1.9 μm up to 4.0 μm (5260 to 2560 cm^{-1}) in the LP01 emission mode. The very high brilliance associated with the collimated laser, high output power (>1.5W), and average spectral power density (up to 0.5 mW/nm) make this all-fiber integrated laser a suitable device for a wide range of micro-beam applications. Although this high-power level is needed to enable and fully use the non-linear processes in the optical fiber, it could damage optical parts, especially the aperture blades, the detector, and the sample. To avoid the potential damage, we used a reflective IR neutral density filter (ND=0.3, NDIR03A, Thorlabs) to decrease the intensity of the source. The Coverage® laser source had been coupled to the Nicolet spectrometer in the Earth Sciences Institute of Orléans, ISTO (Orléans, France) by an in-house designed optical configuration. Due to the high brilliance and collimation of this laser source, an aperture size of 5 \times 5 μm^2 has been reached with a high SNR. The hyperspectral data (rectangular and linear maps) of the SFI were recorded with 2 μm and 1 μm step sizes (smaller than the beam size), respectively.

2.2.4. Setup IV

The mid-infrared microspectroscopy setup in the SMIS beamline was equipped with the same Continuum microscope as the setup II and III coupled to a Nicolet 8700 FTIR spectrometer (Thermo Fisher Scientific, USA). For the infrared source, synchrotron edge radiation from a bending magnet at the SMIS beamline of the SOLEIL Synchrotron Facility was used at the SMIS 2 branch. During the beamtime, the synchrotron emitted at a constant current of 500 mA.^{49, 82} The edge radiation is mainly circularly polarized, but the beam also contains an undefined proportion of bending radiation, which is linearly polarized. The synchrotron radiation is emitted with an angular dependence; longer wavelengths are emitted at higher angles. This may result in chromatic aberrations, especially through high refractive index or birefringent materials. Quartz is a slightly birefringent crystal but the fragment was cut perpendicular to the c axis, so that no effect is expected. Also, the change in the refractive index from quartz to water (and back) is quite limited. Consequently, we expect no chromatic aberrations for the synchrotron measurements.

Due to the high quality (in terms of brilliance and collimation) of the radiation source, an aperture size of $3 \times 3 \mu\text{m}$ was achieved. This IR beam approached the diffraction limit, which is $2.53 \mu\text{m}$ at $2.7 \mu\text{m}$ wavelength (using Abbe equation). For recording the spectral rectangular and linear maps of SFI, the step size was defined as $2 \mu\text{m}$ and $1 \mu\text{m}$, respectively.

3. Results

3.1. Normal, bulk, and interfacial behavior of water

Figure 2 compares the absorption spectra of the normal and bulk water. The spectrum of normal water was recorded on a water film with a thickness of about $1 \mu\text{m}$ deposited between two CaF₂ windows ($13 \text{ mm} \times 2 \text{ mm}$) to avoid any signal saturation. Figure 2 shows the differences between the OH stretching band profile characteristics of normal and bulk water after normalization. As shown, the normal water has a narrower peak (centered around 3400 cm^{-1}) than the bulk water. It is worth noting that the spectra are not saturated, i.e., the raw absorbance values never exceed 1.3 (arb. units), and the transmittance value is 5% at minimum. However, even if this positive value guarantees that the spectrum expresses the IR absorbance dynamics of liquid water, it is small enough to give birth to the small parasitic peaks observed at the top of the OH-stretching band. To avoid altering the spectra with this artefact, while keeping the full meaning of the spectra shapes, the FFT filter method (OriginPro v.2021 software) with 15-20 points within the window was employed to smooth all the spectra affected, namely bulk and normal water.

The spectrum of bulk water recorded in the middle of fluid inclusion is considered as the reference spectral signature of water in this study. Namely, its spectral profile (peak shape and position) will be carefully compared to other spectra recorded along the solid-liquid interface as a function of distance from the quartz boundary. The setup configurations (Table 1) will be evaluated based on their potential to capture the interface signature, which is defined as an additional band appearing in the OH stretching region between 3650 and 3750 cm^{-1} .

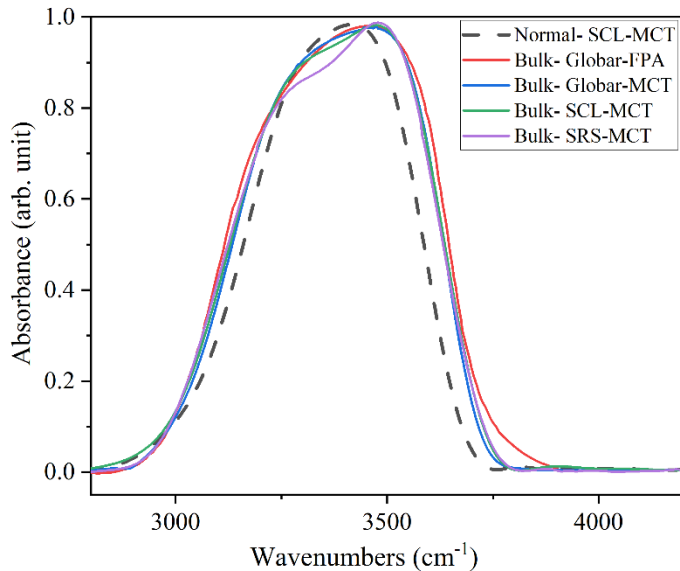


Figure 2. The comparison of the mid-infrared absorption spectra characteristic of normal water (not located inside the fluid inclusion or any closed media) and of bulk water (water located in the center of SFI (micrometric closed media)).

Figure 3 compares the average/representative spectra of the OH stretching band recorded in the middle of SFI (bulk) and near the quartz-water interface using four different experimental setups. Further on, Figure 4 demonstrates that the band shapes and the absorbance values change as a function of the beam location in the SFI, i.e., from the middle (bulk) to the edge (interface). In Figure 4, by showing the series of vertical linear maps across the SFI, the characteristic spectra of quartz, quartz-water interface, and bulk water can be well distinguished.

Setups III and IV, with aperture sizes of $5 \times 5 \mu\text{m}$ and $3 \times 3 \mu\text{m}$, respectively, revealed the presence of the sharp deformation of the water spectrum at ca. 3700 cm^{-1} when approaching the interface. This spectral feature is similar to that previously detected in a water layer within one micrometer of a siloxane-dominated quartz wall.³⁵ On the contrary, this interface signature of water cannot be recorded with setup I or with setup II. Consequently, the SCL and SRS-based setups (Figures 3C and D) allowed us to record the interfacial behavior up to $1 \mu\text{m}$ far from the quartz surface on both sides (symmetric condition). This result proved that exploiting the beam down to the diffraction limit is crucial for recording the interfacial behavior of water molecules.

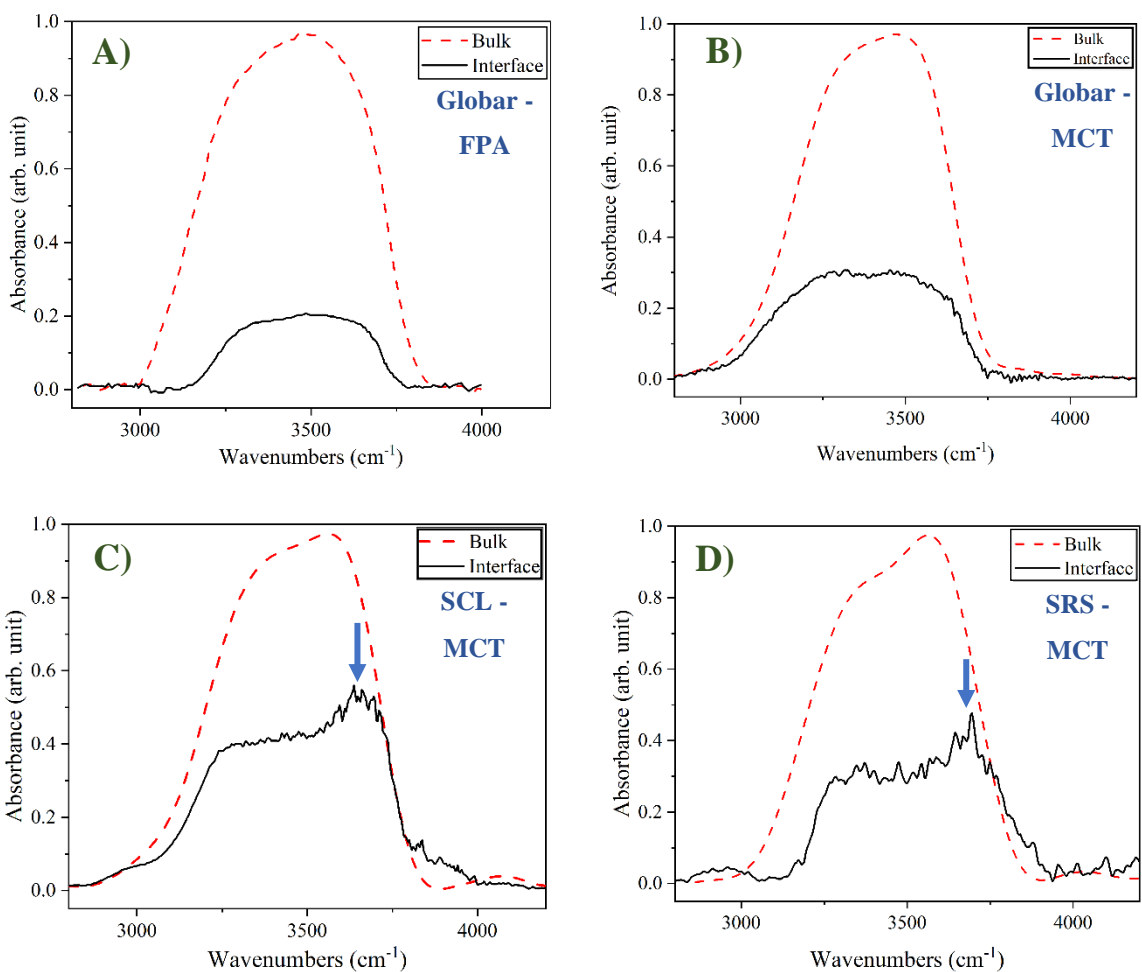


Figure 3. The representative mid-infrared spectra of bulk and interface water (at the quartz boundary) using A) setup I, B) setup II, C) setup III, and D) setup IV. The spectra were normalized and baseline corrected. The arrows show the interfacial signature of water recording with setups III and IV.

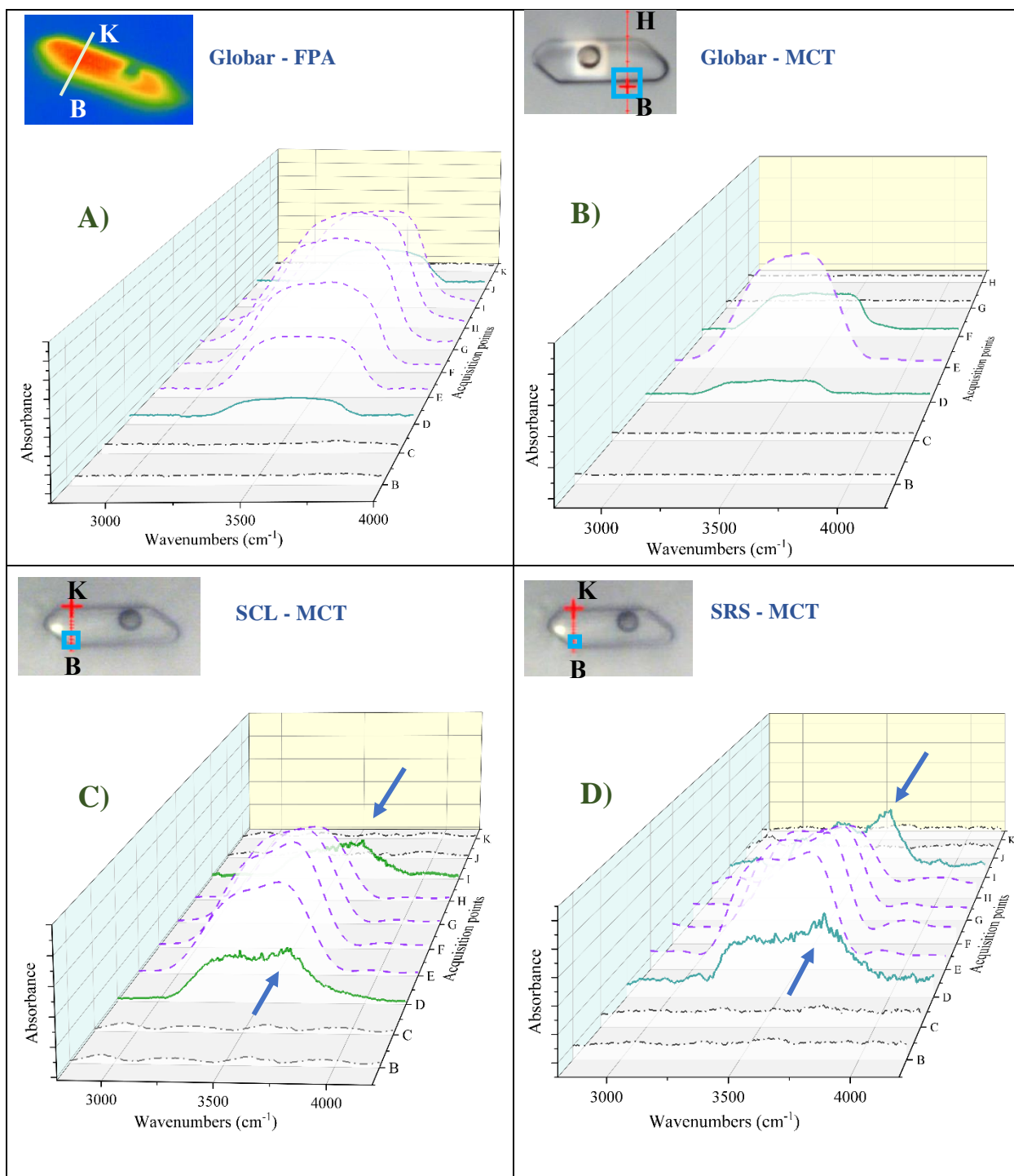


Figure 4. The variation of OH stretching band recorded across the SFI (from point B to point H or K) with A) setup I (aperture-less), B) setup II, C) setup III, and D) setup IV. Black lines (dash-dot line) correspond to quartz, green (solid line) to the near liquid-solid interface, and purple (dash line) to bulk behavior. The blue squares in panels B, C, and D correspond to the aperture size.

3.2. Data processing

The collimation of infrared radiation emerging from a synchrotron and supercontinuum laser offers many significant benefits. However, from a physical point of view, the interaction between a small beam and micrometric objects can create artefacts such as interference fringes, called also sinusoidal waveform or oscillations. Their presence is detrimental since they can be at the origin of incorrect features such as peak shifts, baseline drifts, shoulders, noise, and dispersion in the final spectrum.⁸³ This can be more prominent when one deals with samples such as spheres or rods with sizes similar to the beam size, where Mie-type scattering may occur.^{84, 85} This can significantly affect the SNR of diffraction-limited spatial resolution measurements since scattering may direct the main intensity of the beam out of the confocal aperture.

Probing samples with plane-parallel sides, such as the upper and lower quartz surface in a distance of micrometers in mid-infrared spectroscopy transmission measurements, may lead to multiple reflections of the beam and broad sinusoidal trends in baselines called interference fringes that overlay with chemical spectral features.^{86, 87}

Interference fringes and Mie scattering effect are the two main features observed in the raw spectra, making them challenging to use for their analytical function.^{84, 85, 88-91} Figure 5A shows a sinusoidal baseline with an almost constant period recorded in all our spectra, whereas Figure 6A shows the Mie scattering effect (large and broad undulation of the baseline c.a. 3700 cm⁻¹). The following part will discuss how these two main artifacts can be corrected.

3.2.1. Interference fringes (side-band effect)

As shown in figure 5A, the oscillations are the common physical feature in our mid-infrared microspectroscopy measurements, especially well seen in the case of setups III and IV. The period of the sinusoid can be used to compute the distance between the two semi-reflective surfaces using the following equation: $\Delta\nu = 1 / (2dn)$, where $\Delta\nu$ = the increment in wavenumber between successive interference fringes, d = thickness of the fragment, and n = refractive index of the material.⁹² According to this equation, the thickness of the quartz fragment hosting the SFI can be estimated to $18 \pm 1 \mu\text{m}$, which is in good agreement with its actual thickness according to CT tomography ($19 \pm 1 \mu\text{m}$).

Processing the acquired data is necessary to define and quantify the various absorbance spectrum contributions individually in the hyperspectral data. Some models allow suppressing the interference fringes in FTIR data.^{86, 87, 93, 94} A modified interferogram can suppress interference fringes in the absorption/transmission spectrum by replacing the sinusoidal trend in the interferogram with a horizontal line.⁹⁵ Using the central burst to model and eliminate the side bursts is another approach to directly edit the interferogram for rectification.⁹⁶ There are other correcting methods, which take advantage of the fact that interference fringes have much lower intensity than desired spectral features; therefore, exploiting the filtering techniques either in the spectral domain, such as a series expansion of the spectrum to eliminate low-frequency terms⁹⁷ or

in the Fourier domain⁹⁰ can remove the fringes. Other methods employ a partial least-squares method to eliminate interference fringes and noises.^{78, 98-100}

In this study, the same procedure as Faggini and Hines was applied, which determines the amplitude and period for every fringe in the absorption spectrum.⁷⁸ This procedure first defines sharp and broad absorption features relative to the frequency of the interference fringes. Following this step, we worked on the interferogram, and the frequency of the components related to the interference fringes was identified. After isolating the remaining components with respect to their wavenumber by applying the filtering method, the interferogram was Fourier-transformed to create the pure spectrum of the interference fringes. Finally, the isolated pure interference fringes were subtracted from the original spectrum (Figure 5A). Figure 5B shows the corrected spectra after the data treatment with the software Igor 9.0 for removing the interference fringes and baseline correction with the OriginPro v.2021 (peak analyzer function).

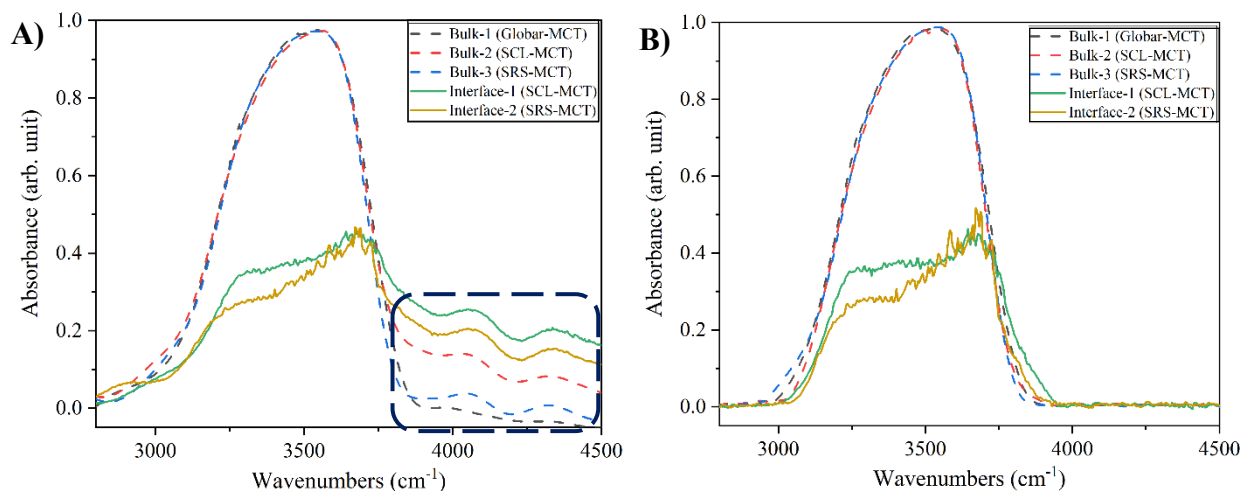


Figure 5. A) Bulk and interface mid-infrared spectra of water recorded with setups II, III, and IV showed the oscillating interference fringes. B) The corrected spectra of bulk and interface water after interference fringes removal processing according to Faggini and Hines's method.⁷⁸

3.2.2. Mie Scattering effect

The phenomenon called Mie scattering was first studied analytically by Gustav Mie, as he presented the mathematical description of light scattering of an electromagnetic plane wave by a homogeneous sphere of arbitrary size.¹⁰¹ Mohlenhoff and Romeo et al. were the first to report on Mie scattering in mid-infrared microspectroscopy of biological cells.^{84, 85} Mie scattering is seen mostly as large and highly non-linear baseline fluctuations in the absorbance spectra. In addition, strong peak distortions are observed since absorption and scattering are highly entangled in Mie-type scattering, where the scattering depends on the complex refractive index whose real part determines the optical properties and the imaginary part to the absorption properties. The real and imaginary part of the refractive index are related through a Kramers-Kronig relation. Mie scattering is particularly pronounced where the surface of an object has a local curvature with a radius that is on the same order of magnitude as the wavelength of the radiation. Practical

approximation theories have been established for the intricate Mie formalism, which captures many important scattering aspects.^{102, 103} Generally, it is necessary to disentangle Mie scattering and other physical effects from the molecular absorption in FTIR absorbance spectra to make conclusions about the chemistry of the samples.

There are several correction methods for handling physical effects in FTIR spectroscopy. The most used is the Extended Multiplicative Signal Correction (EMSC), a flexible approach for correcting FTIR spectra, and in particular, the Mie Extinction EMSC has been used for several cases to remove Mie scattering efficiently.¹⁰⁴⁻¹⁰⁹ Recently, deep learning-based approaches for Mie scattering correction have also been employed to successfully disentangle absorption and scattering contributions in the hyperspectral FTIR data and, in some cases, even outperform the EMSC-based algorithms.^{79, 110}

As seen in Figure 6A, there is a large baseline undulation in the spectra taken in/around the bubble. To correct these spectra, we trained a scatter correction model on simulated spectral data similar manner to Ref.⁷⁹, where a deep learning model is trained to solve the IR spectroscopic inverse scattering problem. We built a deep convolutional neural network (DCNN) to infer the pure absorbance spectra as well as give an estimate of the refractive index and the radius of the curvature on which the light scatters. Then, Figure 6B shows the water spectra in/around the bubble after Mie scattering correction.

The model was trained on data created by simulating IR spectroscopic measurements. Due to the relative simplicity of the IR spectra of water, we trained our model on completely simulated absorbance spectra, where we simulated the water spectra as superpositions of three Gaussian curves. Indeed, decomposing the OH stretching region with three Gaussian components is a very classic scheme,^{111, 112} providing excellent fits of the data with a minimum number of parameters (Okham's razor principle). We created the training data for our DCNN by simulating the bulk water spectra as three Gaussian sub-bands with randomly varying widths and heights and then calculating the scatter-distorted spectra for different spherical scatterers with radii between 2 and 13 microns and refractive index ratios between 0.2 and 1.3 by solving Maxwell's equations and calculating the loss of radiation as the light travels through the sample.^{103, 113} Thereafter, we trained the model to solve the inverse problem and infer the absorbance spectra from the scatter-distorted spectra and the physical properties of the sample. The architecture of the DCNN is essentially the same as in Ref.⁷⁹, apart from the fact that we only have one spectral output channel since we need consider only a single sphere.

After completing training, we have a model that corrects the measured spectra, gives us the absorbance spectra, as well as predicting the radius and refractive index ratio. Thus, it can correct the scattering in the measured spectra in/around the bubble. We also used the corrected spectra and predicted physical parameters and simulate the scatter-distorted spectra to check that this is similar to the measured spectra and thereby demonstrate that our corrected spectra are viable and that Mie scattering can indeed explain the undulations seen in the measured spectra. It is crystal

clear in Figure 6A that the simulated spectra are reasonably similar to the measured spectra in/around the bubble.

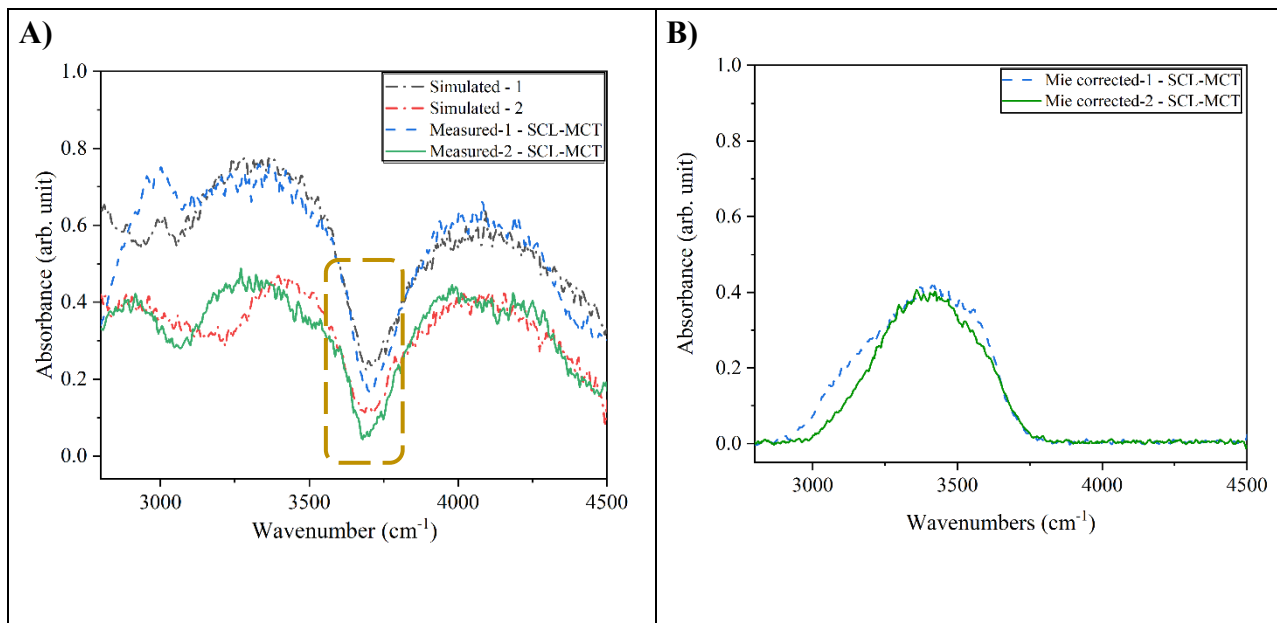


Figure 6. A) The measured and simulated mid-infrared spectra with the Mie scattering effect occurred in/around the bubble (acquired by setup III). B) The spectra after Mie-scattering correction and normalized with respect to the bulk water.

3.2.3. Final spectra after processes

Figure 7 shows the bulk and interface water spectra recorded with setups III and IV after applying the processing methods to eliminate the interference fringes and Mie scattering contributions. As can be seen, both experimental setups with diffraction-limited spatial resolution reveal evident differences between the bulk and interface as well as the presence of the particular spectral signature of water in the vicinity of the micrometric scale solid boundary. It is worth noting that the interfacial contribution is much better detectable after processing. This confirms unambiguously that the origin of the recorded interfacial signature is not related to any scattering effect.

Almost the same spectra of bulk water were recorded using setups III and IV. However, there is a slight discrepancy between the interface signatures. This difference in the spectral profile (shape) can be related to the smaller aperture size and higher spatial resolution provided by setup IV. In this setup, the integrated area of the interface spectrum and its absorption value are lower than those obtained by setup III. Also, it can be related to the geometry of the fluid inclusion, especially near the edges where the beam size is commensurate with the depth of SFI. Nevertheless, the main peak position locates in the same wavenumber (c.a. 3700 cm⁻¹) for both interface spectra (either setup III or IV).

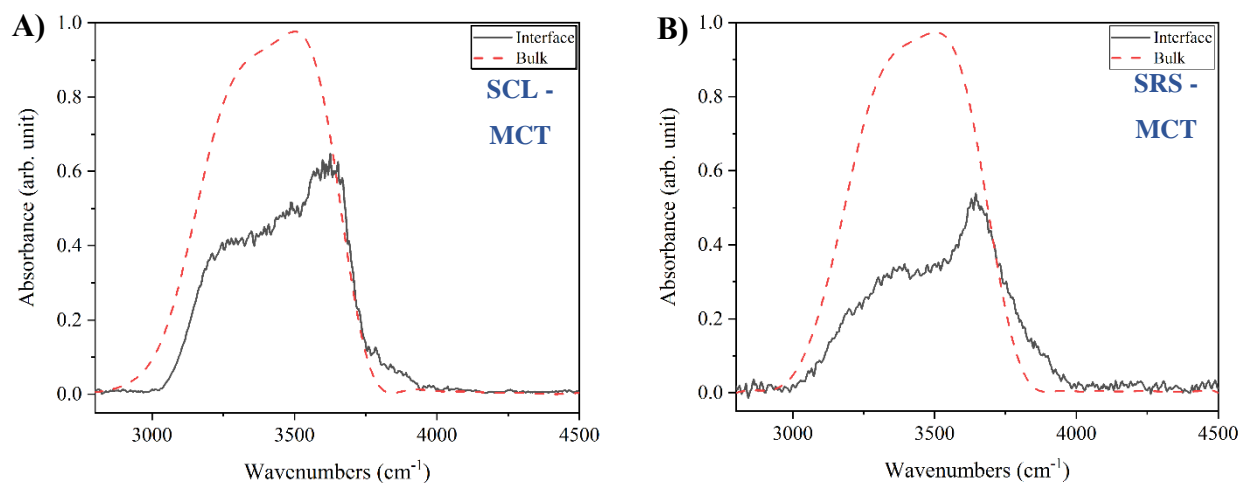


Figure 7. The average/representative mid-infrared spectra of bulk and interface water in the SFI after processing acquired by A) setup III and B) setup IV.

3.3. Hyperspectral absorption maps of SFI

3.3.1. Insight from setup III

A rastered hyperspectral map provides an opportunity to detect the interfacial effect in the SFI and compare the spectra more meticulously as a function of the beam location. Figure 8 shows the rectangular spectral map of SFI recorded with setup III in the laboratory after a few processing steps (baseline correction, normalization, and interference fringes removal). Two different absorbance distribution maps are presented with respect to the two characteristic wavenumbers: i) 3400 cm^{-1} , which corresponds to the bulk signature of water as previously shown in Figure 7A, and ii) 3700 cm^{-1} assigned to the interface signature. As shown in Figure 8, the bulk-like water spectra with maximum absorption values were observed in the middle of inclusion (far from the liquid-solid and liquid-vapor interfaces). Regarding the absorption value in bulk, this value gradually diminished toward the SFI edges, most likely because of reduced water quantity in the SFI borders.

Figure 8A shows the absorbance distribution maps before Mie scattering correction in which the interfacial behavior is observed in/around the bubble and along the quartz boundary. This is related to a large undulation detected at almost the same wavenumber as the interfacial signature (c.a. 3700 cm^{-1}) appearing in/around the bubble, which, as previously shown (Figure 6A), corresponds to the Mie scattering effect. By applying the Mie scattering correction method on all hyperspectral data, the interfacial behavior of water is observed near the quartz boundary, i.e., along the liquid-solid interface, and also around the bubble (water-air interface) (Figure 8B).

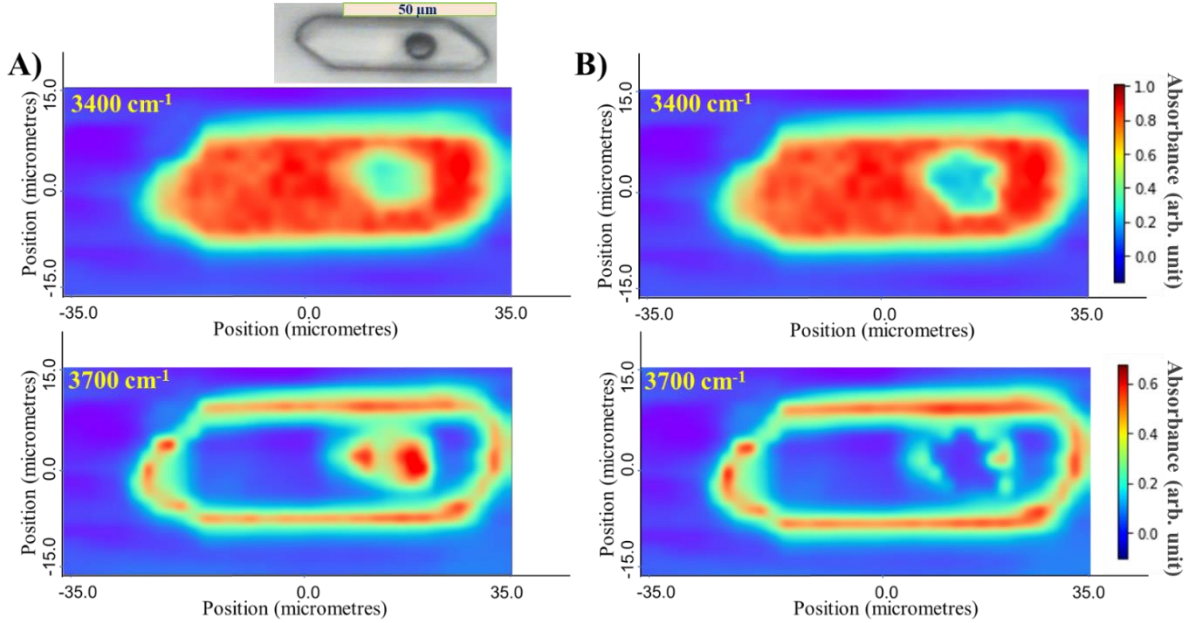


Figure 8. Hyperspectral maps of the SFI acquired by setup III showing the distribution of absorbance at two characteristic wavenumbers: 3400 cm^{-1} related to the bulk and 3700 cm^{-1} representing the interface water behavior A) before and B) after Mie scattering correction.

3.3.2. Insight from setup IV

Hyperspectral maps were also recorded using synchrotron radiation as an IR source. Because of the higher brilliance and collimation, the beam size could be reduced to $3\times 3\text{ }\mu\text{m}$. With this setup, the spectral maps were taken exclusively along the half-left part of the fluid inclusion to avoid undesirable movement of the bubble. It is important to note that high energy and heat transfer of the synchrotron source caused a rapid movement of the bubble when the beam was focused on it. Since the bubble follows the beam location when getting in focus, we tried to avoid approaching too close to the bubble because such a situation significantly masks either the bulk or the interface features. Figure 9 shows the absorbance distribution maps of the half fluid inclusion after processing (baseline correction, normalization, and interference fringes removal) at the two characteristics wavenumbers representing the bulk (c.a. 3400 cm^{-1}) and interface (c.a. 3700 cm^{-1}) water behavior (as shown before in Figure 7B). The interfacial spectral signature appears very sharp due to the higher spatial resolution of this method. As can be seen, there is a good agreement between the hyperspectral maps obtained from setup IV and setup III.

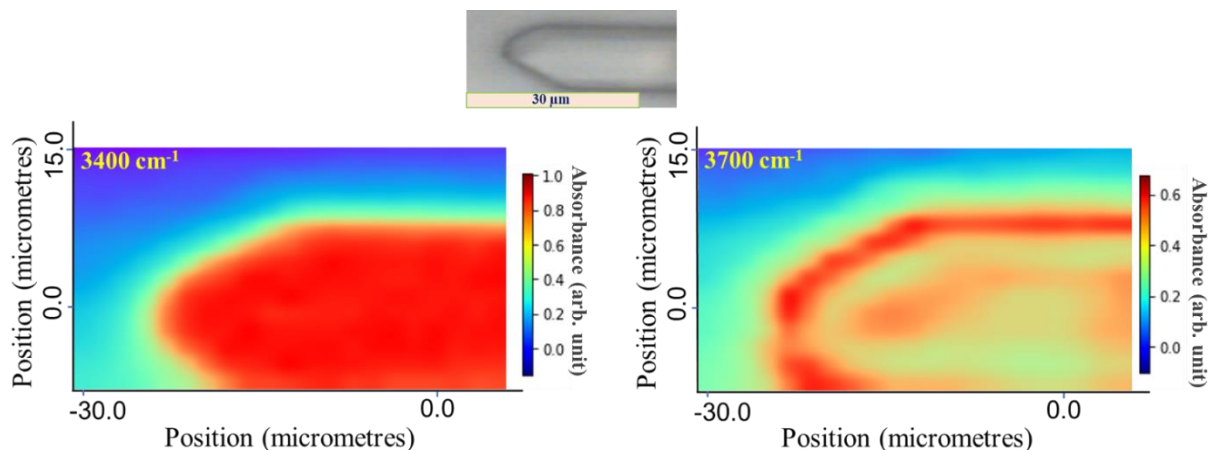


Figure 9. Hyperspectral maps of the SFI acquired by setup IV (synchrotron beam) show the absorbance distribution at two characteristic wavenumbers: 3400 cm^{-1} related to the bulk and 3700 cm^{-1} representing the interface.

4. Discussion

This study aimed to test the performance of four FTIR experimental setups (Table 1) applied to SFI (trapped water inside a quartz cavity) to detect micrometer-scale interface-imprinted spectral features. According to the presented results, setup IV employing a synchrotron radiation source allowed to record the sharpest, well-resolved band near 3700 cm^{-1} , which is unambiguous evidence of the specific behavior of water near the quartz-water interface. This is related to the high spatial resolution down to the diffraction limit (equal to $2.53\text{ }\mu\text{m}$ at $2.7\text{ }\mu\text{m}$ wavelength) offered by the synchrotron source coupled to the confocal microscope. Our results are consistent with those of Bergonzi's, which revealed for the first time the specific interfacial behavior of water molecules at the micrometric scale along a solid wall.³⁵

This is worth noting that almost the same results were recorded by setup III, based on the mid-infrared fiber-based supercontinuum laser that allowed to achieve beam size of $5\times 5\text{ }\mu\text{m}$ in the laboratory condition. These results are coherent with previous ones,^{51,56} which revealed the ability of supercontinuum laser sources to perform high-resolution micro-FTIR measurements.

In contrast, the FPA images obtained from setup I did not allow to record the interface signature accurately because the interface domain is smaller than the actual spatial resolution of the system. Nevertheless, the aperture-less microscope with the FPA detector allows substantially faster data gathering at a spatial resolution two or three times bigger than the diffraction limit. These results confirm previous experiments, which demonstrated that the FPA detector may not always be suitable for exploring the chemical or physical features at the diffraction limit.⁷⁰ This may be counterintuitive as the area on the sample covered by each detector element has a dimension below the diffraction limit. However, because of the diffraction, each detector element receives a contribution from an area bigger than the area on the sample nominally covered by each element.

The microscope aperture of a confocal microscope employing synchrotron-based radiation or a supercontinuum laser source allows to control of the spatial resolution at the diffraction limit and consequently records the interfacial signature. In the FPA detector-equipped microscope, physical apertures do not limit the IR beam illuminating region. Instead, the projected image of the unmasked IR beam on the sample is collected using an array of IR detector components; therefore, the precision of aperture-less images is highly dependent on the optical system magnification and numerical aperture.^{70, 114, 115}

The experiments performed in this study demonstrate that FTIR technique applied in the diffraction limit resolution can be used to study the water behavior in the micrometric fluid inclusion. The water behavior and corresponding spectra are highly affected as a function of beam location toward the quartz and the gas bubble; however, they are partly affected by optical issues, such as interference fringes and Mie scattering. The former corresponds to the thickness of the quartz fragment, and the latter relates to the shape of the bubble. All these phenomena can overlay with chemical spectral features and may cast doubt that such signatures are a general feature which have a systematic significance for the water-solid interphase as a whole. That is why two different methods were applied to suppress these trends. After processing the data, the variation of the overall band shape has been emphasized, making clear that an additional peak at ca. 3700 cm^{-1} takes place systematically in the vicinity of the quartz boundary. The existence of two contributions at 3400 cm^{-1} and 3700 cm^{-1} can be assigned to the difference in H-bonding due to the fact that the properties of solid surface is known to alter the H-bonding structure of water at interfaces.¹¹⁶⁻¹²⁰

As mentioned earlier, the variation in the H-bonding near the interfaces in general is commonly investigated by nonlinear vibrational spectroscopic techniques, like SHG or SFG.^{36, 37} The SFG measurement on hydrophilic surfaces revealed the presence of two peaks at 3250 cm^{-1} and 3450 cm^{-1} , leading to conclude that the water network is locally ordered close to a hydrophilic solid surface.³⁸⁻⁴⁰ On the contrary, the peak between 3650 and 3750 cm^{-1} can be attributed either to isolated silanol groups⁴¹ or in the case of water near to hydrophobic surface can be corresponded to free OH groups.^{39, 42, 44, 45, 121} In our case, the OH stretching bands of normal and bulk water show a strong lower wavenumber component (c.a. 3400 cm^{-1}), and they do not have a shoulder at higher wavenumbers (c.a. 3700 cm^{-1}), which is coherent with previous studies.^{35, 112, 122} A band detected between 3650 and 3750 cm^{-1} , visible along the quartz boundary (water-quartz interface), can be assigned to the absorption of weakly hydrogen bonded water molecules near the hydrophobic surface.^{35, 123, 124} Indeed, the silica can form either a hydrophilic or hydrophobic surface with respect to the ratio of siloxane bridge (Si-O-Si) to silanol groups (Si-O-H).¹²⁵ However, we did not record the distinct peak (i.e., separated from the OH stretching band) c.a. 3700 cm^{-1} similar to SFG measurements but we observed an additional peak as a band broadening within the stretching modes of water. As a consequence, the peak is not interpreted as detecting a pure free OH (dangling OH) mode, but assigned to an enrichment of interfacial water in the less-connected water molecules. In this way of reasoning, this interfacial behavior and the disruption

between the water H-bonding might be originated from an hydrophobic character of quartz and active surface forces like the hydrophobic force emanating from the surface and causing the disorganization (chaotropic effect) of water molecules,³⁵ over a distance that has never been recorded up to now.

5. Conclusion

In this study, the interfacial behavior of water in synthetic fluid inclusion was investigated by high-resolution mid-infrared microspectroscopy measurements in transmission mode. The OH stretching region of water molecules (3000 to 3800 cm^{-1}) was recorded with four different setups to test the potential of beam at the diffraction limit for detecting the spectral features along the interface. We observed two undesirable trends in our raw data related to interference fringes and Mie scattering. These trends can be a common problem in the case of a micrometric-scale object like fluid inclusion. We applied the filtering algorithm and deep learning-based models for the interference fringes and Mie scattering to suppress these physical effects and correct the spectra.

According to the results, two main parameters play a major role in the high-resolution mid-infrared microspectroscopy: the optical arrangement of the microscope and the infrared source. Regarding the optical arrangement of microscopes, the confocal mode with dual path single aperture configuration connected to the single-element MCT detector has a higher efficiency in terms of spatial resolution compared to the aperture-less microscope connected to the FPA detector.

After conducting the experiments with three different infrared sources (Globar, SCL, and SRS), the hyperspectral data of the synthetic fluid inclusion proved the ability of setup III based on the supercontinuum laser (aperture size = $5 \times 5 \mu\text{m}$), coupled to the confocal microscope, and equipped with the MCT to record the interfacial behavior of water. The interfacial behavior of water has been observed with a vibrational signature between 3650 and 3750 cm^{-1} . These high-resolution measurements revealed that the vibrational energy of water changes over a significant thickness from the quartz boundary (solid-liquid interface). The acquired data are consistent with the synchrotron measurements, which were recorded by the aperture size equal to $3 \times 3 \mu\text{m}$.

Therefore, the supercontinuum laser can be considered an alternative to a synchrotron source to obtain a high brilliance and collimated broadband infrared source in the MIR with a high spatial resolution. This feature can make the laser a suitable source in the mid-infrared microspectroscopy setups for conducting high-resolution measurements down to the diffraction limit, especially in the field of geoscience and porous media, where a smaller beam size than the pore size is required to record the chemical composition or physical features of the pore.

Acknowledgments

This work has received financial support from the French Agency for Research (Agence Nationale de la Recherche) through the Labex Voltaire ANR-10-LABX-100-01 and the Equipex Planex ANR-11-EQPX-36. This study benefits from the SOLEIL Synchrotron allocation n° 20211104. The authors thank Dr. Frederic Jamme and Prof. Sophie Le Caër for the insightful discussions in processing and analyzing the data. Also, we would like to express our deep gratitude toward Prof. Melissa A. Hines's for her generous help with the interference fringe correction method. Esteban Le Moing and Frédéric Savoie from ISTO's workshop are kindly thanked for their help with the house-in coupling of supercontinuum laser to FTIR spectrometer. We are finally grateful to the Editor, Nicole Pamme, and to two anonymous reviewers, who greatly helped us to improve the initial manuscript.

Reference

1. J. Katok, A. Sommer and P. L. Lang, *Applied Spectroscopy Reviews*, 1989, 25, 173-211.
2. C. Sandt, J. Frederick and P. Dumas, *Journal of biophotonics*, 2013, 6, 60-72.
3. S. Clède, C. Policar and C. Sandt, *Applied Spectroscopy*, 2014, 68, 113-117.
4. O. Klementieva, K. Willén, I. Martinsson, B. Israelsson, A. Engdahl, J. Cladera, P. Uvdal and G. Gouras, *Nature communications*, 2017, 8, 1-9.
5. C. Sandt, C. Nadaradjane, R. Richards, P. Dumas and V. Sée, *Analyst*, 2016, 141, 870-883.
6. W. André, C. Sandt, P. Dumas, P. Djian and G. Hoffner, *Analytical Chemistry*, 2013, 85, 3765-3773.
7. A. Paulus, A. Engdahl, Y. Yang, A. Boza-Serrano, S. Bachiller, L. Torres-Garcia, A. Svanbergsson, M. G. Garcia, G. K. Gouras and J.-Y. Li, *International journal of molecular sciences*, 2021, 22, 3430.
8. T. M. Pereira, D. M. Zezell, B. Bird, M. Miljković and M. Diem, *Analyst*, 2013, 138, 7094-7100.
9. J. Meneghel, S. Passot, F. Jamme, S. Lefrançois, P. Lieben, P. Dumas and F. Fonseca, *Analytical and Bioanalytical Chemistry*, 2020, 412, 7049-7061.
10. C. Modugno, C. Peltier, H. Simonin, L. Dujourdy, F. Capitani, C. Sandt and J.-M. Perrier-Cornet, *Frontiers in Microbiology*, 2020, 10, 3122.
11. M. Igisu, Y. Ueno, M. Shimojima, S. Nakashima, S. M. Awramik, H. Ohta and S. Maruyama, *Precambrian Research*, 2009, 173, 19-26.
12. T. C. Hazen, E. A. Dubinsky, T. Z. DeSantis, G. L. Andersen, Y. M. Piceno, N. Singh, J. K. Jansson, A. Probst, S. E. Borglin and J. L. Fortney, *Science*, 2010, 330, 204-208.
13. A. de Anchieta Câmara Jr, P.-A. Maréchal, R. Tourdot-Maréchal and F. Husson, *Food microbiology*, 2019, 79, 137-146.

14. A. Skoczen, Z. Setkowicz, K. Janeczko, C. Sandt, F. Borondics and J. Chwiej, *Spectrochimica Acta Part A: Molecular and Biomolecular Spectroscopy*, 2017, 184, 13-22.
15. C. Saulou, F. Jamme, L. Girbal, C. Maranges, I. Fourquaux, M. Cocaign-Bousquet, P. Dumas and M. Mercier-Bonin, *Analytical and bioanalytical chemistry*, 2013, 405, 2685-2697.
16. A. A. Câmara Jr, T. D. Nguyen, R. Saurel, C. Sandt, C. Peltier, L. Dujourdy and F. Husson, *Frontiers in Microbiology*, 2020, 11, 899.
17. T. D. Nguyen, S. Guyot, C. Pénicaud, S. Passot, C. Sandt, F. Fonseca, R. Saurel and F. Husson, *Frontiers in Microbiology*, 2020, 11, 1887.
18. S. Passot, J. Gautier, F. Jamme, S. Cenard, P. Dumas and F. Fonseca, *Analyst*, 2015, 140, 5920-5928.
19. T. Nguyen, S. Guyot, C. Pénicaud, S. Passot, C. Sandt, F. Fonseca, R. Saurel and F. Husson, *Analyst*, 2017, 142, 3620-3628.
20. J. P. Cain, P. L. Gassman, H. Wang and A. Laskin, *Physical Chemistry Chemical Physics*, 2010, 12, 5206-5218.
21. C. Gasaway, M. Mastalerz, F. Krause, C. Clarkson and C. Debuhr, *Journal of Microscopy*, 2017, 265, 60-72.
22. Y. Chen, L. D. Caro, M. Mastalerz, A. Schimmelmann and A. Blandón, *Journal of microscopy*, 2013, 249, 69-81.
23. S. Bertarione, F. Bonino, F. Cesano, S. Jain, M. Zanetti, D. Scarano and A. Zecchina, *The Journal of Physical Chemistry B*, 2009, 113, 10571-10574.
24. Z. Li, E. A. Henriksen, Z. Jiang, Z. Hao, M. C. Martin, P. Kim, H. L. Stormer and D. N. Basov, *Nature physics*, 2008, 4, 532-535.
25. Y. Zhang, T.-T. Tang, C. Girit, Z. Hao, M. C. Martin, A. Zettl, M. F. Crommie, Y. R. Shen and F. Wang, *Nature*, 2009, 459, 820-823.
26. T. Astruc, F. Peyrin, A. Vénien, R. Labas, M. Abrantes, P. Dumas and F. Jamme, *Food chemistry*, 2012, 134, 1044-1051.
27. R. Vaskoska, A. Vénien, M. Ha, J. D. White, R. R. Unnithan, T. Astruc and R. D. Warner, *Food Chemistry*, 2021, 343, 128544.
28. M. Motoyama, A. Vénien, O. Loison, C. Sandt, G. Watanabe, J. Sicard, K. Sasaki and T. Astruc, *Food chemistry*, 2018, 248, 322-329.
29. A. J. King, P. F. Schofield, N. R. Stephen, M. D. Frogley, G. Cinque and S. S. Russell, *Infrared Physics & Technology*, 2018, 94, 244-249.
30. A. R. Nichols and R. Wysoczanski, *Chemical Geology*, 2007, 242, 371-384.
31. M. K. Nieuwoudt, M. P. Simpson, M. Tobin and L. Puskar, *Vibrational Spectroscopy*, 2014, 75, 136-148.
32. N. Guilhaumou and P. Dumas, *Oil & Gas Science and Technology*, 2005, 60, 763-779.

33. Y. Chen, C. Zou, M. Mastalerz, S. Hu, C. Gasaway and X. Tao, *International journal of molecular sciences*, 2015, 16, 30223-30250.
34. G. Della Ventura, F. Bellatreccia, A. Marcelli, M. Cestelli Guidi, M. Piccinini, A. Cavallo and M. Piochi, *Analytical and bioanalytical chemistry*, 2010, 397, 2039-2049.
35. I. Bergonzi, L. Mercury, P. Simon, F. Jamme and K. Shmulovich, *Physical Chemistry Chemical Physics*, 2016, 18, 14874-14885.
36. E. H. Backus, J. Schaefer and M. Bonn, *Angewandte Chemie International Edition*, 2021, 60, 10482-10501.
37. F. Tang, T. Ohto, S. Sun, J. r. m. R. Rouxel, S. Imoto, E. H. Backus, S. Mukamel, M. Bonn and Y. Nagata, *Chemical reviews*, 2020, 120, 3633-3667.
38. S. Kataoka, M. C. Gurau, F. Albertorio, M. A. Holden, S.-M. Lim, R. D. Yang and P. S. Cremer, *Langmuir*, 2004, 20, 1662-1666.
39. Y. R. Shen and V. Ostroverkhov, *Chemical reviews*, 2006, 106, 1140-1154.
40. Z. Pászti and L. Guzzi, *Vibrational Spectroscopy*, 2009, 50, 48-56.
41. L. Dalstein, E. Potapova and E. Tyrode, *Physical Chemistry Chemical Physics*, 2017, 19, 10343-10349.
42. E. Tyrode and J. F. Liljeblad, *The Journal of Physical Chemistry C*, 2013, 117, 1780-1790.
43. S. Strazdaite, J. Versluis, E. H. Backus and H. J. Bakker, *The Journal of Chemical Physics*, 2014, 140, 054711.
44. S. E. Sanders and P. B. Petersen, *The Journal of Chemical Physics*, 2019, 150, 204708.
45. O. Isaienko and E. Borguet, *Langmuir*, 2013, 29, 7885-7895.
46. F. Jamme, B. Lagarde, A. Giuliani, G. Garcia and L. Mercury, *Journal of Physics: Conference Series*, 2013, 425, 142002.
47. G. Carr, *Review of Scientific Instruments*, 2001, 72, 1613-1619.
48. G. Carr, *Vibrational Spectroscopy*, 1999, 19, 53-60.
49. P. Dumas, F. Polack, B. Lagarde, O. Chubar, J. Giorgetta and S. Lefrançois, *Infrared Physics & Technology*, 2006, 49, 152-160.
50. M. C. Martin, U. Schade, P. Lerch and P. Dumas, *TrAC Trends in Analytical Chemistry*, 2010, 29, 453-463.
51. J. Kilgus, G. Langer, K. Duswald, R. Zimmerleiter, I. Zorin, T. Berer and M. Brandstetter, *Optics express*, 2018, 26, 30644-30654.
52. G. Williams, *Handbook of Vibrational Spectroscopy*, 2006, DOI: <https://doi.org/10.1002/0470027320.s0212>.
53. J. Chalmers, N. Everall and M. Chesters, *Analyst*, 1998, 123, 579-586.

54. G. Carr, L. Miller and P. Dumas, in *Biomedical Applications of Synchrotron Infrared Microspectroscopy*, 2010, DOI: <https://doi.org/10.1039/9781849731997-00226> pp. 226-259.
55. L. M. Miller and R. J. Smith, *Vibrational spectroscopy*, 2005, 38, 237-240.
56. F. Borondics, M. Jossent, C. Sandt, L. Lavoute, D. Gaponov, A. Hideur, P. Dumas and S. Février, *Optica*, 2018, 5, 378-381.
57. I. Lindsay, S. Valle, J. Ward, G. Stevens, M. Farries, L. Huot, C. Brooks, P. M. Moselund, R. Vinella and M. Abdalla, *Optical Biopsy XIV: Toward Real-Time Spectroscopic Imaging and Diagnosis*, 2016, 9703, 15-23.
58. M. J. Nasse, M. J. Walsh, E. C. Mattson, R. Reininger, A. Kajdacsy-Balla, V. Macias, R. Bhargava and C. J. Hirschmugl, *Nature methods*, 2011, 8, 413-416.
59. P. Bassan, M. J. Weida, J. Rowlette and P. Gardner, *Analyst*, 2014, 139, 3856-3859.
60. K. Yeh and R. Bhargava, *Biomedical Vibrational Spectroscopy 2016: Advances in Research and Industry*, 2016, 9704, 17-23.
61. I. Zorin, P. Gattinger, A. Ebner and M. Brandstetter, *Optics Express*, 2022, 30, 5222-5254.
62. S. Dupont, C. Petersen, J. Thøgersen, C. Agger, O. Bang and S. R. Keiding, *Optics express*, 2012, 20, 4887-4892.
63. C. R. Petersen, N. Prtljaga, M. Farries, J. Ward, B. Napier, G. R. Lloyd, J. Nallala, N. Stone and O. Bang, *Optics letters*, 2018, 43, 999-1002.
64. L. Lavoute, C. Sandt, F. Borondics, N. Ducros and S. Février, *Optica Publishing Group (specialty Optical Fibers)*, 2016, DOI: <https://doi.org/10.1364/SOF.2016.SoTu2G.5>, SoTu2G. 5.
65. M. R. Kole, R. K. Reddy, M. V. Schulmerich, M. K. Gelber and R. Bhargava, *Analytical chemistry*, 2012, 84, 10366-10372.
66. Y.-P. Tseng, P. Bouzy, C. Pedersen, N. Stone and P. Tidemand-Lichtenberg, *Biomedical Optics Express*, 2018, 9, 4979-4987.
67. M. J. Hackett, S. Caine, X. Liu, T. E. May and F. Borondics, *Vibrational Spectroscopy*, 2015, 77, 51-59.
68. B. R. Wood, M. Kiupel and D. McNaughton, *Veterinary pathology*, 2014, 51, 224-237.
69. J. Nallala, M.-D. Diebold, C. Gobinet, O. Bouché, G. D. Sockalingum, O. Piot and M. Manfait, *Analyst*, 2014, 139, 4005-4015.
70. C. Sandt, Z. Dionnet, M. Toplak, E. Fernandez, R. Brunetto and F. Borondics, *Journal of Spectral Imaging*, 2019, 8.
71. S. Bratos, J.-C. Leicknam, G. Gallot and H. Ratajczak, in *Ultrafast Hydrogen Bonding Dynamics and Proton Transfer Processes in the Condensed Phase*, Springer, 2002, pp. 5-30.
72. R. Rundle and M. Parasol, *The Journal of Chemical Physics*, 1952, 20, 1487-1488.

73. K. Nakamoto, M. Margoshes and R. Rundle, *Journal of the American Chemical Society*, 1955, 77, 6480-6486.
74. V. R. Hande and S. Chakrabarty, *The Journal of Physical Chemistry B*, 2022, 126, 1125-1135.
75. V. R. Hande and S. Chakrabarty, *Physical Chemistry Chemical Physics*, 2016, 18, 21767-21779.
76. K. I. Shmulovich and C. M. Graham, *Contributions to Mineralogy and Petrology*, 2004, 146, 450-462.
77. D. Schiering, T. Tague Jr, J. Reffner and S. Vogel, *Analisis*, 2000, 28, 46-52.
78. M. F. Faggin and M. A. Hines, *Review of scientific instruments*, 2004, 75, 4547-4553.
79. E. A. Magnussen, B. Zimmermann, U. Blazhko, S. Dzurendova, B. Dupuy–Galet, D. Byrtusova, F. Muthreich, V. Tafintseva, K. H. Liland and K. Tøndel, *Communications Chemistry*, 2022, 5, 175.
80. J. P. Blitz and D. G. Klarup, *Journal of chemical education*, 2002, 79, 1358.
81. J. M. Dudley, G. Genty and S. Coen, *Reviews of modern physics*, 2006, 78, 1135.
82. G. Santoro, I. Yousef, F. Jamme, P. Dumas and G. Ellis, *Review of Scientific Instruments*, 2011, 82, 033710.
83. J. M. Chalmers, *Handbook of vibrational spectroscopy*, 2006, DOI: <https://doi.org/10.1002/0470027320.s3101>.
84. B. Mohlenhoff, M. Romeo, M. Diem and B. R. Wood, *Biophysical journal*, 2005, 88, 3635-3640.
85. A. Kohler, J. Sule-Suso, G. Sockalingum, M. Tobin, F. Bahrami, Y. Yang, J. Pijanka, P. Dumas, M. Cotte and D. Van Pittius, *Applied spectroscopy*, 2008, 62, 259-266.
86. T. Konevskikh, A. Ponossov, R. Blümel, R. Lukacs and A. Kohler, *Analyst*, 2015, 140, 3969-3980.
87. G. Azarfar, E. Aboualizadeh, N. M. Walter, S. Ratti, C. Olivieri, A. Norici, M. Nasse, A. Kohler, M. Giordano and C. J. Hirschmugl, *Analyst*, 2018, 143, 4674-4683.
88. A. Ibrahim, A. Predoi-Cross and P. M. Teillet, *AIP Conference Proceedings*, 2010, 1214, 97-99.
89. D. L. Kingsbury and P. L. Marston, *JOSA*, 1981, 71, 358-361.
90. A. M. Pistorius and W. J. DeGrip, *Vibrational spectroscopy*, 2004, 36, 89-95.
91. Q. Fu and W. Sun, *Applied Optics*, 2001, 40, 1354-1361.
92. S. Croll and A. Skaja, *Journal of Coatings Technology*, 2003, 75, 85-94.
93. T. G. Mayerhöfer, S. Pahlow, U. Hübner and J. Popp, *Analyst*, 2020, 145, 3385-3394.

94. J. H. Solheim, F. Borondics, B. Zimmermann, C. Sandt, F. Muthreich and A. Kohler, *Journal of Biophotonics*, 2021, 14, e202100148.
95. G. Mellau and B. Winnewisser, *Laboratory and Astronomical High Resolution Spectra*, 1995, 81, 138.
96. D. A. Naylor, A. A. Schultz and T. A. Clark, *Applied optics*, 1988, 27, 2603-2607.
97. A. H. Lipkus, *Applied spectroscopy*, 1988, 42, 395-400.
98. B. Hren, J. Mink and L. Balazs, *Analytical chemistry*, 2002, 74, 6402-6407.
99. T. Iwata and J. Koshoubu, *Applied spectroscopy*, 1994, 48, 1453-1456.
100. T. Iwata and J. Koshoubu, *Applied spectroscopy*, 1996, 50, 747-752.
101. G. Mie, *Ann. Phys*, 1908, 25, 0003-3804.
102. H. Van de Hulst, Inc., New York, 1957, 470.
103. P. Walstra, *British Journal of Applied Physics*, 1964, 15, 1545.
104. A. Kohler, C. Kirschner, A. Oust and H. Martens, *Appl. Spectrosc*, 2005, 59, 707-716.
105. H. Martens, J. P. Nielsen and S. B. Engelsen, *Analytical Chemistry*, 2003, 75, 394-404.
106. M. A. Brandsrud, R. Blümel, J. H. Solheim and A. Kohler, *Scientific reports*, 2021, 11, 1-14.
107. T. Konevskikh, R. Lukacs, R. Blümel, A. Ponossov and A. Kohler, *Faraday discussions*, 2016, 187, 235-257.
108. J. H. Solheim, E. Gunko, D. Petersen, F. Großerüschkamp, K. Gerwert and A. Kohler, *Journal of biophotonics*, 2019, 12, e201800415.
109. P. Bassan, A. Kohler, H. Martens, J. Lee, H. J. Byrne, P. Dumas, E. Gazi, M. Brown, N. Clarke and P. Gardner, *Analyst*, 2010, 135, 268-277.
110. E. A. Magnussen, J. H. Solheim, U. Blazhko, V. Tafintseva, K. Tøndel, K. H. Liland, S. Dzurendova, V. Shapaval, C. Sandt and F. Borondics, *Journal of Biophotonics*, 2020, 13, e202000204.
111. I. Bergonzi, L. Mercury, J.-B. Brubach and P. Roy, *Physical Chemistry Chemical Physics*, 2014, 16, 24830-24840.
112. J.-B. Brubach, A. Mermet, A. Filabozzi, A. Gerschel and P. Roy, *The Journal of chemical physics*, 2005, 122, 184509.
113. C. F. Bohren and D. R. Huffman, *Absorption and scattering of light by small particles*, John Wiley & Sons, 2008.
114. E. N. Lewis, P. J. Treado, R. C. Reeder, G. M. Story, A. E. Dowrey, C. Marcott and I. W. Levin, *Analytical chemistry*, 1995, 67, 3377-3381.

115. Z. Dionnet, A. Aléon-Toppani, F. Borondics, R. Brunetto, A. Buellet, Z. Djouadi, A. King, S. Rubino and D. Troadec, *Microscopy and Microanalysis*, 2018, 24, 2100-2101.
116. E. Breynaert, M. Houlleberghs, S. Radhakrishnan, G. Grübel, F. Taulelle and J. A. Martens, *Chemical Society Reviews*, 2020, 49, 2557-2569.
117. G. Gonella, E. H. Backus, Y. Nagata, D. J. Bonthuis, P. Loche, A. Schlaich, R. R. Netz, A. Kühnle, I. T. McCrum and M. T. Koper, *Nature Reviews Chemistry*, 2021, 5, 466-485.
118. T. Hayashi, *Chemistry Letters*, 2021, 50, 1173-1180.
119. J. Monroe, M. Barry, A. DeStefano, P. Aydogan Gokturk, S. Jiao, D. Robinson-Brown, T. Webber, E. J. Crumlin, S. Han and M. S. Shell, *Annual Review of Chemical and Biomolecular Engineering*, 2020, 11, 523-557.
120. M. Maccarini, *Biointerphases*, 2007, 2, MR1-MR15.
121. S. Strazdaite, J. Versluis and H. J. Bakker, *The Journal of chemical physics*, 2015, 143, 084708.
122. D. A. Schmidt and K. Miki, *The journal of physical chemistry A*, 2007, 111, 10119-10122.
123. M. A. Henderson, *Surface Science Reports*, 2002, 46, 1-308.
124. A. J. Hopkins and G. L. Richmond, *Applied spectroscopy*, 2013, 67, 261-273.
125. J. D. Cyran, M. A. Donovan, D. Vollmer, F. Siro Brigiano, S. Pezzotti, D. R. Galimberti, M.-P. Gageot, M. Bonn and E. H. Backus, *Proceedings of the national academy of sciences*, 2019, 116, 1520-1525.